Available online at www.sciencedirect.com
ScienceDirect
Earth and Planetary Science Letters 266 (2008) 303–315
EPSL
www.elsevier.com/locate/epsl

Spatial variability of erosion rates inferred from the frequency distribution of cosmogenic ^{3}He in olivines from Hawaiian river sediments

Eric Gayer, Sujoy Mukhopadhyay *, Brendan J. Meade

Department of Earth and Planetary Sciences, Harvard University, 20 Oxford Street, Cambridge, MA 02138, United States

Received 3 May 2007; received in revised form 5 November 2007; accepted 5 November 2007
Available online 22 November 2007
Editor: R.W. Carlson

Abstract

To constrain the spatial distribution of erosion rates in the Waimea river watershed, on the western side of the island of Kauai, Hawaii, we calculate the frequency distribution of cosmogenic ^{3}He concentrations ($[^{3}He]_c$) from helium isotopic measurements in olivine grains from a single sample of river sediment. Helium measurements were made in 26 aliquots of ~30 olivine grains each. The average $[^{3}He]_c$ from the 26 aliquots was used to estimate a basin-wide average erosion rate of 0.056 mm/yr, a value that is similar to erosion rates obtained from geochemical analyses of river sediments from tectonically stable landforms. However, forward models of cosmogenic nuclide production and sediment generation rates are inconsistent with the hypothesis that the observed $[^{3}He]_c$ frequency distribution is the result of a homogeneous, basin wide, erosion rate. Instead, a distribution of erosion rates, from ~0 to 4 mm/yr, may account for the observed frequency distribution. The distribution of erosion rates can be modeled by both non-linear slope- and curvature-dependent erosion rates with power law exponents ranging from 2.0 to 2.5. However, the spatial distribution of cosmogenic nuclides for slope- and curvature-dependent erosion rates are distinct, and we propose strategies to test further the extent to which erosion rates are controlled by the macroscale topographic features. These results demonstrate that the observed frequency distribution of cosmogenic nuclide concentrations in river sediments, combined with numerical modeling of erosion rates, can provide constraints on both the spatial variability of erosion rates in a drainage basin and the form of parameterized erosion laws.

Keywords: cosmogenic nuclides; erosion laws; frequency distribution; helium; Hawaii; topography

1. Introduction

Rates of sediment generation and transport may act as a limiting mechanism for a variety of geomorphic processes, from the hillslope evolution to controlling the surface area available for chemical weathering, which directly affects the interaction between climate, erosion, and tectonics (Molnar and England, 1990; Whipple, 2004; Whipple and Meade, 2004). Techniques used to infer denudation rates include gauging of river loads and measurements of cosmogenic ^{10}Be in river sediments.

* Corresponding author. Tel.: +1 617 496 6441; fax: +1 617 495 8839.
E-mail address: sujoy@eps.harvard.edu (S. Mukhopadhyay).

0012-821X/$ - see front matter © 2007 Elsevier B.V. All rights reserved.
doi:10.1016/j.epsl.2007.11.019

Cosmogenic nuclides are formed primarily by spallation reactions between high-energy neutrons and the major elements in rock. Because neutron flux is attenuated by interaction with matter, the nuclide production rate increases with altitude and decreases with depth in rock. Production of cosmogenic nuclides is only significant within the upper 2 m of the Earth's crust. Thus, the concentration of cosmogenic nuclides in near surface rocks is set by the balance between cosmogenic production and mass removal rates (Lal, 1991). Over the past decade, numerous studies have determined ^{10}Be concentrations in river sediments to constrain basin-averaged erosion rates over catchment areas ranging from 1 to 10^5 km^2, with erosion rates ranging from 0.01 to 0.3 mm/yr (e.g., Brown et al., 1995b; Granger et al., 1996; Riebe et al., 2000; Schaller et al., 2001; Matmon et al., 2003a,b).

The concentration of cosmogenic nuclides in detrital river sediments has been used to investigate relationships between erosion rates and macroscale features of the landscape, such as relief. A correlation between relief and erosion rate has been documented, with high relief areas, in general, eroding at higher rates (Brown et al., 1995b; Granger et al., 1996; Riebe et al., 2000; Schaller et al., 2001; Matmon et al., 2003a,b; Niemi et al., 2005). The relationship between relief and erosion rate, however, has not been quantified rigorously. Further, relief by itself does not control erosion rates. Rather, hillslopes, or hill curvatures, are the parameters that control erosion rate. In the Fort Sage Mountains of California, Granger et al. (1996) observed a correlation between hillslope gradients and catchment-averaged erosion rates, determined from ^{10}Be in detrital quartz. Granger et al. (1996) suggested that erosion rates may have a non-linear dependence on hillslope gradients, although they concluded that the exact relationship between hillslope gradient and erosion rates could not be quantified with their data. In contrast, Matmon et al. (2003a) observed that basin-scale erosion rates in the Great Smoky Mountains scaled linearly with the mean slope of the catchment area. In a study from the Sierra Nevada, Riebe et al. (2000) showed that the average erosion rate in basins that were affected by tectonic faulting is correlated with the average slope gradients. In contrast, average erosion rates in catchments that were removed from the influence of active tectonics showed no correlation with the average hillslope gradients. Riebe et al. (2000) attributed this to the fact that the landscape may have reached erosional equilibrium and hence, steep and gentle slopes were eroding at the same rate. However, correlating catchment-averaged erosion rates with catchment-averaged slopes may not elucidate a relationship, if erosion rates have a non-linear dependence on hillslope gradients.

An alternative approach to investigate how hillslopes, or hill curvatures drive sediment generation rates would be to investigate the relationship between the spatial distribution of slopes and the spatial variability of erosion rates, within an individual catchment area. While distribution of slopes within a catchment area can be readily investigated using a digital elevation map (DEM), virtually no information is available on the distribution of erosion rates within an individual basin to test for a relationship between slope, or curvature, and erosion rates. Here, we present a new approach to both measuring and modeling cosmogenic nuclide concentrations in river sediments that allow us to constrain the spatial distribution of erosion rates within a catchment area. Our technique is based on constructing a frequency distribution from measurements of cosmogenic nuclides in river sediments. We also demonstrate that the frequency distribution of cosmogenic nuclides can place powerful constraints on the form of parameterized erosion laws.

2. Geological setting, sampling strategy, and measurement techniques

We measured cosmogenic ^{3}He concentrations ($[^3\mathrm{He}]_c$) in olivine rich river sands from the Waimea watershed, located in the western part of the island of Kauai, Hawaii, which comprises the Waimea river and its tributaries (Fig. 1). These rivers flow on the tholeiitic shield-building and caldera-fill lavas of the Olokele and Makaweli members that range in age from 4.2 to 3.95 Ma (McDougall, 1979; Clague and Dalrymple, 1988). The sample under investigation, KA9, is a river sediment collected on the bank of the Waimea River at an elevation of 25 m (21°59′24″N, 200°19′48″E; Fig. 1). The drainage area at the sample location is 130 km^2, constituted by the Waimea River and three of its tributaries (Poomau, Koale and Waialae River, Fig. 1). The maximum elevation of the basin is 1416 m on the Olokele plateau, where precipitation rates average 250–750 cm/yr (NOAA National Climatic Data Center). Precipitation rates decrease dramatically in the western half of the Waimea Canyon, averaging 60–75 cm/yr along the western and southwestern rim of the canyon. Precipitation rates at sea-level, at the mouth of the basin, average 50 cm/yr. We selected this study area because the drainage basin has a single lithology, measurement of $[^3\mathrm{He}]_c$ is a well developed technique, and cosmogenic ^{3}He has the highest production rate, allowing for concentration measurements to be made on relatively small numbers of olivine grains.

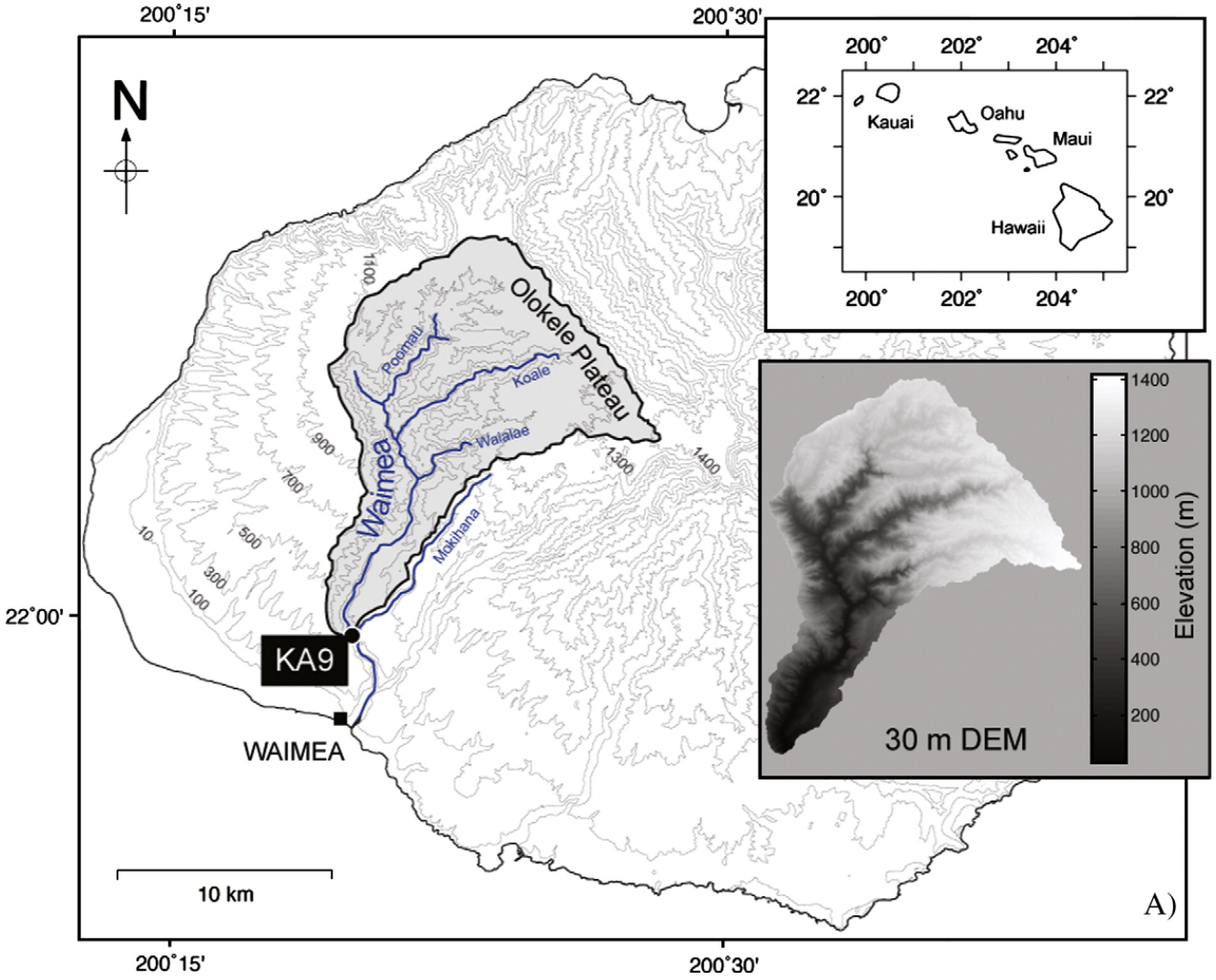

Fig. 1. Topographic map of the Island of Kauai showing the location of the sampled river sand KA9, and the delineation of the Waimea River basin.

Approximately 3 kg of river sediment was collected. Following sieving of the sediment sample to a grain size between 1 and 3 mm, a Nd-B hand magnet was used to remove a large fraction of the sediment that was magnetic, concentrating olivine grains in the residual sediment. Olivine grains free from adhering matrix were handpicked under a binocular microscope and then leached in 1% oxalic acid for 45–60 min at 90 °C to remove surficial alteration. The crystals were then ultrasonically cleaned in distilled water and acetone at room temperature for 10 min. Finally, olivine crystals were divided into 26 aliquots of approximately 30 grains each. The number of grains/aliquot was selected to obtain a signal to blank ratio of ~10, or larger, during the helium isotopic measurements.

To separate $[^3He]_c$ from magmatic ^3He trapped in fluid and melt inclusions, the olivine grains were first crushed under vacuum with a piston crusher. The evolved gases were sequentially exposed to a hot and cold SAES getter and then trapped onto a cryogenic cold-finger at 12 K. Helium was separated from neon at 32 K and inlet into a Nu Noblesse noble gas mass spectrometer. Helium isotopic ratios and concentrations were determined by normalizing to a standard with a $^3He/^4He$ of 8.8 R_A (where R_A is the $^3He/^4He$ ratio normalized to the atmospheric ratio of 1.39×10^{-6}) that was prepared at Harvard (HH3). The HH3 standards analyzed for this study had ^4He abundances that ranged from 2.6×10^{10} atoms to 1.3×10^{11} atoms. ^4He was measured using a Faraday cup and ^3He was measured using a discrete dynode multiplier operating in pulse counting mode. Following crushing, the olivine powders were wrapped in tantalum foil and heated in a vacuum furnace at ~1500 °C for 25 min. The use of tantalum foil allows us to keep the furnace clean, which ensures low procedural blanks for ^3He and ^4He. We routinely performed repeat extractions to ensure complete extraction of He during the initial heating. The vacuum furnace is equipped with two automated liquid nitrogen

traps to keep the backgrounds in the purification line low. Furnace operations and gas handling are completely automated in the Harvard laboratory, allowing for rapid determination of He concentration and isotopic ratios in a large number of samples. Gas handling procedures and mass spectrometric techniques were identical to those used during sample crushing.

Typical ^{3}He and ^{4}He crush blanks were 3.8×10^3 and 4×10^8 atoms, which were <1% and ~2% of the measured signals respectively. Typical furnace blanks for ^{3}He and ^{4}He were 7.8×10^3 and 8×10^8 atoms respectively, averaging 3% and 14% of the sample signals. The total variation in blanks seen during the course of the analyses was 20% for ^{3}He and 15% for ^{4}He, which were taken to be the uncertainties in the blank correction. The reproducibility of HH3 of similar size to the samples was 2% for ^{3}He/^{4}He ratios and <1% for ^{4}He concentrations. The uncertainties in the computed ratios and concentrations are based on the reproducibility of HH3 and the uncertainties associated with the blank correction.

The concentrations of $[^3\mathrm{He}]_c$ in the samples were computed from the following relationships:

$$^3\mathrm{He_c} = {}^3\mathrm{He_{melt}} - {}^3\mathrm{He_{magmatic}} \quad (1)$$

$$\text{and } {}^3\mathrm{He_{magmatic}} = {}^4\mathrm{He_{melt}} \times \left(\frac{^3\mathrm{He}}{^4\mathrm{He}}\right)_{\mathrm{crush}} \quad (2)$$

where $^3\mathrm{He}_c$ is the cosmogenic ^{3}He concentration, $^{3,4}\mathrm{He}_{\mathrm{melt}}$ are the ^{3}He and ^{4}He concentrations determined by fusing the crushed powders, $^3\mathrm{He}_{\mathrm{magmatic}}$ is the inherited magmatic component, and $(^3\mathrm{He}/^4\mathrm{He})_{\mathrm{crush}}$ is the ^{3}He/^{4}He ratio obtained by crushing the olivine grains. The average 1σ uncertainty in $^3\mathrm{He}_{\mathrm{melt}}$ and $^3\mathrm{He}_{\mathrm{magmatic}}$ is 4%. The above correction for inherited magmatic ^{3}He, however, assumes that no radiogenic ^{4}He or nucleogenic ^{3}He is present in the samples and insignificant cosmogenic ^{3}He is present in the fluid/melt inclusions. The U and Th abundances in olivines are extremely low (≪0.01 ppm) (Kurz et al., 1996). To calculate the amount of radiogenic in-growth in the olivines, we assume a melt-olivine partition coefficient of 2×10^{-5} and 5×10^{-5} for U and Th respectively (Beattie 1993; Kennedy et al., 1993). The melt is assumed to have 0.3 ppm U and 1 ppm Th, which is towards the high-end of measured concentrations in Hawaiian tholeiites. The above parameters suggest that over 4.5 Myrs radiogenic in-growth would lead to a ^{4}He concentration of 2.6×10^8 at/g (atoms/g), which is <1% (range 0.6–0.8%) of the measured ^{4}He signals during sample fusion. The olivine crystals analyzed in this study were leached with 1% oxalic acid. From the mass loss during leaching, and assuming a spherical geometry for the grains, we calculate that on average a 50 μm thick rind from the olivine crystals was removed. Since the stopping distance for an α-particle is ~20 μm, implantation of α-particles into the olivines from the matrix is not a feasible source of the measured ^{4}He during sample fusion.

The reaction $^6\mathrm{Li}(n,\alpha)^3\mathrm{H}\rightarrow{}^3\mathrm{He}$ could be a potential source of nucleogenic ^{3}He in olivines. Since the olivine grains in the sediments are derived from different flows, and because the flows may have different U and Th abundances, an exact calculation of the nucleogenic ^{3}He content is not possible. Rather, we decided to calculate an upper limit of the nucleogenic ^{3}He content. The Li concentrations of mantle derived olivines range from <1 ppm to 10 ppm (Ryan and Langmuir, 1987; Kent and Rossman, 2002) and for our computations we use 10 ppm as the Li abundance in olivines. U and Th concentration in the basalt matrix is assumed to 0.3 ppm and 1 ppm respectively. We assume that no B or Gd is present in the matrix. Since these elements are very efficient neutron absorbers, our calculations provide an upper limit on the amount of nucleogenic ^{3}He production. Using the methodology developed by Andrews (1985), the nucleogenic ^{3}He in the olivines would be 2.8×10^4 at/g after 4.5 Myrs. The calculated nucleogenic ^{3}He averages 1.5% (range 0.6–6%) of the cosmogenic $[^3\mathrm{He}]_c$ contents. Thus, we conclude that neither radiogenic ^{4}He nor nucleogenic ^{3}He are present in the samples at a significant level. This is consistent with previous observations of cosmogenic helium, but not radiogenic or nucleogenic helium in olivines from Kauai (Scarsi, 2000; Mukhopadhyay et al., 2003).

3. Cosmogenic ^{3}He and constraints on basin-wide erosion rates

Helium concentrations and isotopic ratios are summarized in Table 1. ^{3}He/^{4}He ratios obtained by crushing the olivine grains range from 16.2 to 26.4 R_A. ^{3}He/^{4}He ratios obtained by fusing the crushed powders range from 24.6 to 105.7 R_A. For all the 26 aliquots, the fused powders had ^{3}He/^{4}He ratios that were higher than the crush ratios, clearly demonstrating the presence of cosmogenic ^{3}He. $[^3\mathrm{He}]_c$ ranges from $0.43\pm0.15\times10^6$ to $4.07\pm0.34\times10^6$ at/g with a weighted average concentration of 1.65×10^6 at/g. The uncertainty in $[^3\mathrm{He}]_c$ was computed by propagating the uncertainty in $^3\mathrm{He}_{\mathrm{magmatic}}$ and $^3\mathrm{He}_{\mathrm{melt}}$ through Eq. (1).

The mean $[^3\mathrm{He}]_c$ can be used to estimate an average erosion rate for the Waimea basin. Assuming isotopic steady state, whereby the production of ^{3}He is balanced by erosional loss, (Lal and Arnold, 1985; Lal, 1991;

Table 1
Cosmogenic He concentration in the 26 aliquots of olivine grains

Sample	No. of grains	Crush step		Melt step			
		Weight (g)	$(^3He/^4He)_{crush}$ (R_A)	Weight (g)	$(^3He/^4He)_{melt}$ (R_A)	$[^4He]_{melt}$ (10^{10} at/g)	$[^3He]_c$ (10^6 at/g)
KA9-1	32	0.1006	22.1±0.3	0.0733	46.0±2.4	7.2±0.3	2.4±0.3
KA9-2	36	0.1036	19.8±0.7	0.0793	35.2±1.8	6.6±0.3	1.4±0.2
KA9-3	38	0.1012	21.6±0.7	0.0876	28.6±1.5	8.7±0.2	0.8±0.3
KA9-4	30	0.0998	20.8±0.6	0.0811	57.1±3.0	4.8±0.2	2.4±0.3
KA9-5	31	0.1034	19.8±0.3	0.0858	35.1±1.8	6.0±0.3	1.3±0.2
KA9-6	33	0.1034	19.3±0.8	0.0866	54.3±2.8	5.6±0.3	2.7±0.3
KA9-7	31	0.1007	24.5±0.6	0.0828	30.8±1.6	9.5±0.3	0.8±0.2
KA9-8	31	0.1003	22.6±0.8	0.0791	31.2±1.6	9.9±0.2	1.2±0.3
KA9-9	37	0.1046	20.4±0.6	0.0847	30.1±1.6	6.6±0.3	0.9±0.2
KA9-10	36	0.1019	26.4±0.2	0.0731	42.7±2.2	5.0±0.2	1.1±0.2
KA9-11	31	0.1018	19.4±0.5	0.0820	24.6±1.3	8.1±0.4	0.6±0.2
KA9-12	24	0.1003	17.0±0.5	0.0830	36.6±1.9	7.3±0.2	2.0±0.3
KA9-13	31	0.1029	18.7±0.2	0.0838	36.0±1.9	5.4±0.3	1.3±0.2
KA9-14	27	0.1024	19.9±1.0	0.0787	26.6±1.4	4.7±0.2	0.4±0.1
KA9-15	29	0.1020	19.8±1.0	0.0825	41.6±2.2	5.4±0.3	1.6±0.2
KA9-16	26	0.1031	25.9±0.4	0.0786	64.4±3.4	4.7±0.2	2.0±0.2
KA9-17	24	0.1015	22.7±0.5	0.0819	89.3±4.7	5.4±0.3	4.1±0.4
KA9-18	27	0.1023	23.9±0.5	0.0821	59.0±3.1	3.7±0.2	2.5±0.3
KA9-19	25	0.1011	16.2±1.3	0.0817	105.7±5.5	4.4±0.2	3.9±0.3
KA9-20	36	0.0996	21.3±1.4	0.0732	40.4±2.1	5.2±0.3	1.5±0.2
KA9-21	32	0.1007	21.4±0.7	0.0810	33.9±1.8	3.2±0.2	2.0±0.4
KA9-22	38	0.1010	21.7±1.0	0.0793	26.7±1.4	5.8±0.3	0.5±0.2
KA9-23	36	0.1006	17.8±1.3	0.0843	43.7±2.3	11.5±0.2	2.0±0.3
KA9-24	29	0.1031	20.7±1.8	0.0922	46.0±2.4	6.9±0.2	1.4±0.2
KA9-25	39	0.1006	21.1±1.0	0.0893	34.1±1.8	5.5±0.2	1.0±0.2
KA9-26	40	0.1025	23.9±0.3	0.0901	38.4±2.0	6.1±0.2	1.2±0.3

R_A is the $^3He/^4He$ ratio normalized to the atmospheric ratio of 1.39×10^{-6}. Reported uncertainties are 1σ and uncertainties in $^3He/^4He$ ratios and He concentrations were computed from the reproducibility of standards as well as from uncertainties in blank correction. $[^3He]_c$ is the concentration of cosmogenic ^3He and uncertainties in $[^3He]_c$ was computed by propagating uncertainties in $^3He_{magmatic}$ and $^3He_{melt}$ through Eq. (1).

Brown et al., 1995a) the average erosion rate across the drainage area (Lal, 1991; Brown et al., 1995b) is given by:

$$\varepsilon = \frac{\Lambda P}{N\rho} \tag{3}$$

where N (at/g) is the mean concentration of the cosmogenic nuclide in the river sediment, P (at/g/yr) is the production rate of the cosmogenic nuclide averaged over the entire basin, Λ (g/cm^2) the attenuation length, ρ (g/cm^3) the density, and ε (cm/yr) is the erosion rate.

To calculate the basin-averaged erosion rate, we use a basalt density of 3 g/cm^3, an attenuation length of 160 g/cm^2 (Kurz, 1986a; Sarda et al., 1993), and a high latitude sea-level production rate of 125 at/g/yr, as scaled from cosmogenic ^3He measurements in basalts from Hawaii (Kurz et al., 1990). Using a 30m digital elevation map (DEM) of the Waimea basin (http://hawaii.wr.usgs.gov/kauai/data.html), and altitude and latitude scaling factors from Lal (1991), we calculated the $[^3He]_c$ production rate of each pixel. The production rate of each pixel was corrected for azimuthally dependent topographic shielding effects using the methodology described by Dunne et al. (1999) and Niemi et al. (2005). The $[^3He]_c$ production rate averaged over the entire basin is 175 at/g/yr, which yields an average erosion rate of 0.056 mm/yr.

4. Observed frequency distribution and the spatial variability of erosion rates

A large range of $[^3He]_c$ concentrations is observed in the 26 aliquots of olivine grains (Fig. 2). We ask the question: Can the frequency distribution of $[^3He]_c$ be consistent with a uniform erosion rate over the entire basin? The production rate of a cosmogenic nuclide increases with altitude, approximately exponentially, and a distribution of $[^3He]_c$ in individual olivine grains should be expected even if the entire Waimea basin is eroding at a uniform rate of 0.056 mm/yr. However, each of our aliquots averages $[^3He]_c$ over ~30 grains, and the range of $[^3He]_c$ among the different aliquots should be significantly less than the parent population of olivine

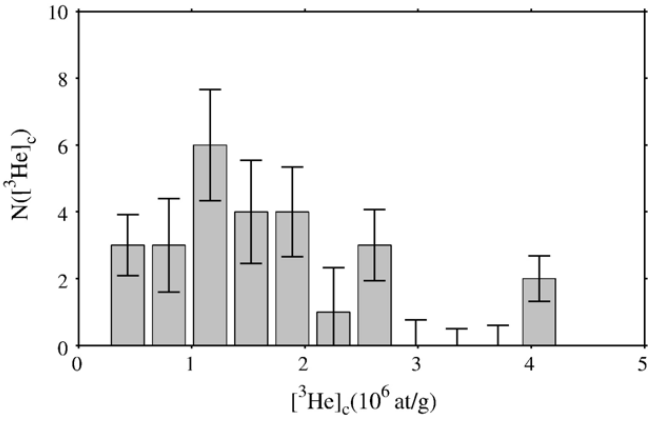

Fig. 2. Frequency distribution of the 26 ^3He_c concentrations. The error bars represent the 1σ uncertainty in the frequency distribution. Error bars were calculated based on the uncertainty in individual ^3He_c concentrations (Table 1) and from 1000 Monte Carlo simulations.

grains. Alternatively, the observed frequency distribution could reflect spatial variability in erosion rates over the basin. Hence, to interpret the observed frequency distribution, we generated model frequency distributions of $[^3He]_c$ for our sampling site (KA9; Fig. 1) based on assumed erosion functions. We investigated three erosion laws: 1) a uniform erosion rate over the entire basin, 2) erosion rate as a function of local topographic slope, and 3) erosion rate as a function of the local topographic curvature. For all three erosion laws we assume that sediment storage on hillslopes or along the river channel results in negligible buildup of $[^3He]_c$, compared to $[^3He]_c$ produced *in-situ* in the rock. The modeled $[^3He]_c$ frequency distributions are then compared with the observed distributions to place constraints on the erosion rate distribution. Our observed frequency distribution was constructed from ^3He measurements on a small number of olivine grains that were sampled stochastically from a larger parent distribution. Hence, to interpret the observed frequency distribution and facilitate meaningful comparisons between the observed and modeled frequency distributions, we need to understand the statistical variability that is to be expected by calculating the mean concentration of 30 olivine grains 26 times. To this end, for each erosion function, the model $[^3He]_c$ concentrations were calculated based on 1000 Monte Carlo simulations, which allows us to put confidence intervals on the probability of finding a sample distribution that fits the one observed.

4.1. Frequency distribution model using a constant erosion rate in the drainage area

We first evaluate whether the observed frequency distribution is consistent with the entire Waimea basin eroding at a uniform erosion rate that is equal to the mean erosion rate of 0.056 mm/yr. We used a 30 m digital elevation model (DEM) of the island of Kauai to generate the model erosion rate distribution. The 30 m DEM was selected since tests show that model results are not significantly different between 10 m and 30 m DEMs. We also assume that the olivine grains are uniformly distributed in the bedrock, so that each pixel in the DEM serves as a potential source location (PSL) of a detrital olivine grain. The assumption is based on the fact that flows in the Waimea basin are olivine rich (Mukhopadhyay et al., 2003), individual flow thicknesses are on the order of a 1–5 m, and our DEM resolution is 30 m. The calculation of the model ^3He frequency distributions can be broken into three steps. In step one, we calculated $[^3He]_c$ in each pixel using a constant erosion rate of 0.056 mm/yr across the basin. The $[^3He]_c$ production rate for each pixel was scaled for altitude (Lal, 1991) and topographic shielding (Section 3). In step two, 30 pixels were randomly picked from the DEM and $[^3He]_c$ for the pixels were averaged to simulate the ^3He measurement of an aliquot of 30 olivine grains. Since we are assuming a uniform erosion rate, every PSL contributes detrital olivine grains to the sediment budget at the same rate and hence, every pixel has the same probability of being selected. In step three, the process of randomly selecting 30 pixels and averaging $[^3He]_c$ was repeated 26 times to simulate the 26 aliquots of $[^3He]_c$ measurements.

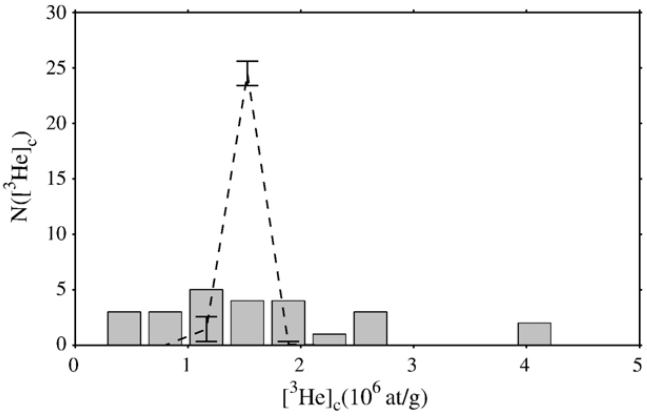

Fig. 3. Comparison between the synthetic frequency distribution based on a constant erosion rate of 0.056 mm/yr over the entire drainage area and the observed $[^3He]_c$ distribution. The black dashed line represents the average value of 1000 simulations, and the bars represent the 67% confidence interval. The model distribution shows a very restricted range of $[^3He]_c$, and does not extend to either the low, or high, $[^3He]_c$ values measured in the olivine grains. Thus, it differs visibly from the observed frequency distribution. Moreover, over the 1000 simulations we did not observe a single run that remotely matched the measured $[^3He]_c$ distribution. Hence, we rule out the scenario of a constant erosion rate over the entire Waimea basin.

The modeled frequency distributions from the numerical simulations are compared with the observed frequency distribution in Fig. 3. It is obvious that assuming a uniform erosion rate over the entire basin results in a very poor fit between the model and observed frequency distribution. In particular, $[^3He]_c$ in the model distribution has a well defined mode and does not show either the low or high extremes in $[^3He]_c$ measured in the olivine grains. We can, therefore, rule out the possibility that the entire Waimea basin is eroding at a constant rate. The simple forward model presented here indicates that to match the observed frequency distribution the parent population of olivine grains must have a significantly wider distribution of $[^3He]_c$ than predicted by a constant erosion rate over the entire basin.

4.2. Frequency distribution model using slope- and curvature-dependent erosion functions

Compared to the case of spatially uniform erosion in the Waimea basin, spatially variable erosion rates can yield a wider range of $[^3He]_c$ in the olivine grains sampled at site KA9 (Figs. 1 and 2). If erosion rates are dependent on the topographic slope, or curvature, spatial variability in erosion rates is expected. Previous studies have discussed the form of parameterized erosion rules that relate sediment generation and transport to topographic slope (e.g., Whipple and Tucker, 1999), and curvature (e.g., Fernandes and Dietrich, 1997). Here we explore the consequences of assuming slope- and curvature-dependent sediment generation laws for the distribution of $[^3He]_c$ in olivine grains at the KA9 sampling site.

We express the erosion laws as simple power law functions of slope,

$$\varepsilon = a\left(\sqrt{\left(\frac{dz}{dx}\right)^2+\left(\frac{dz}{dy}\right)^2}\right)^b \tag{4}$$

or curvature,

$$\varepsilon = c\left(\sqrt{\left(\frac{d^2z}{dx^2}\right)^2+\left(\frac{d^2z}{dy^2}\right)^2}\right)^d \tag{5}$$

where ε is the erosion rate of each pixel, z is the elevation of each pixel, a and c are coefficients of erosion, and b and d are the power–law exponents that determine how erosion rates scale with topographic gradients. The topographic slope and curvature are computed directly from the DEM. The strategy we used to constrain values for a–b and c–d was to assume values for these constants, and test if the modeled $[^3He]_c$ frequency distributions generated by assuming either a slope- or curvature-dependent erosion law was a fit to the measured frequency distribution. To generate the model distributions, we first calculate the theoretical $[^3He]_c$ expected for each pixel of the DEM using (i) the $[^3He]_c$ production rate corrected for topographic shielding (Section 3) and (ii) an erosion rate calculated from assumed values of a–b, or c–d (Eqs. (4) and (5)). Next, we randomly select 30 pixels from the DEM. However, because we now assume non-uniform erosion rates over the basin, an erosion rate dependent sampling function was introduced in the algorithm, since regions with higher erosion rate contribute more sediment than regions that erode more slowly. The stochastic sampling function weights the probability, P, of selecting a pixel to its erosion rate, $P(\varepsilon)_i = \varepsilon_i / \sum_{j=1}^{n} \varepsilon_j$ where n is the total number of pixels in the DEM.

The model frequency distribution, N_{mod} (^3He_c), was classified as a good fit to the observed frequency distribution, $N_{\mathrm{obs}}(^3He_c)$, if the goodness of fit parameter, R, was <0.67, and R is defined as:

$$R = \frac{\sum_{i=1}^{n} |N^i_{\mathrm{obs}} - N^i_{\mathrm{mod}}|}{\sum_{i=1}^{n} |N^i_{\mathrm{obs}}|} \tag{6}$$

where n is the total number of bins. While the goodness of fit criteria is arbitrary, it accounts for at least a third of the power in the measured frequency distribution, allows for the visualization of the sensitivity of predicted frequency distributions to model parameters, and admits a wide enough range of models to understand the probability of randomly drawing a detrital sample similar to that analyzed here.

Figs. 4 and 5 show the parameter space mapped for the slope (a–b) and curvature (c–d) dependent erosion function, respectively, as well as the probability of obtaining a good fit to the measured frequency distribution for particular values of the slope and curvature coefficients. If sediment generation was slope dependent in the Waimea basin, the probability of obtaining a good fit to the observed frequency distribution is >75% for a restricted range of slope exponents, b, between 2 and 2.5, with a corresponding a value of ~0.01. Outside of this range of a–b values, the probability of obtaining a good fit to the observed distribution falls off dramatically. Fig. 4B shows the comparison between the model frequency distribution generated using our best estimate of the values of a and b, $a=0.01$ and $b=2.23$. These values of a and b resulted in the highest percentage of good fits (85%) over the 1000 Monte Carlo simulations and imply erosion rates in the

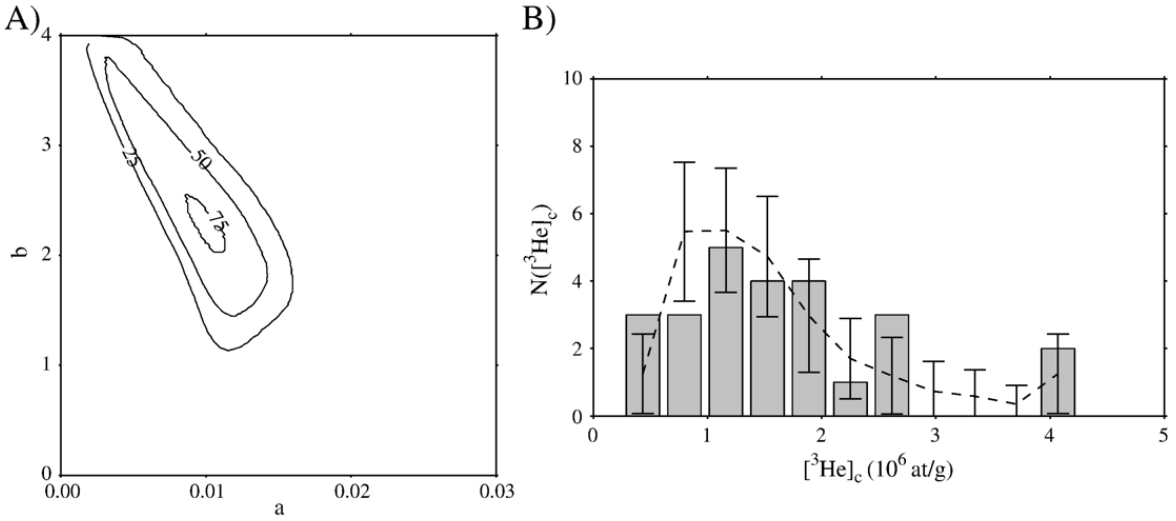

Fig. 4. Frequency distribution modeled using a slope-dependent erosion function. A) The range of a and b values explored correspond to the entire scale of the x- and y-axis. For each run, a synthetic distribution of $[^3He]_c$ was generated and the distribution was classified as a good fit if it accounted for at least a third of the power in the measured frequency distribution (see text for explanation). The contours represent the percentage of model runs that were classified as a good fit to the observed frequency distribution for a particular value of a and b. B) Comparison between the observed frequency distribution (histogram in gray) and the modeled frequency distribution (black dashed line) using our best estimate of $a=0.01$ and $b=2.23$ for Eq. (4). The estimate is based on the largest number of good fits (85%) over the 1000 simulations. The dotted line represents the mean values of each bin from the 1000 Monte Carlo simulations, and the bars represent the corresponding 67% confidence interval.

Waimea basin range from ~0 to 3.3 mm/yr across the basin, with a mean erosion rate of 0.053 mm/yr. Thus, unlike the case of uniform erosion rate, a slope-dependent erosion function, with a slope exponent of ~2–2.5 is consistent with the observed frequency distribution.

Curvature-dependent sediment generation may also be consistent with our ^{3}He measurements from site KA9 (Fig. 5). In this case, good fits to the observed frequency distribution can be obtained for a wide range of c values but only a limited range of the curvature exponent, d, at a

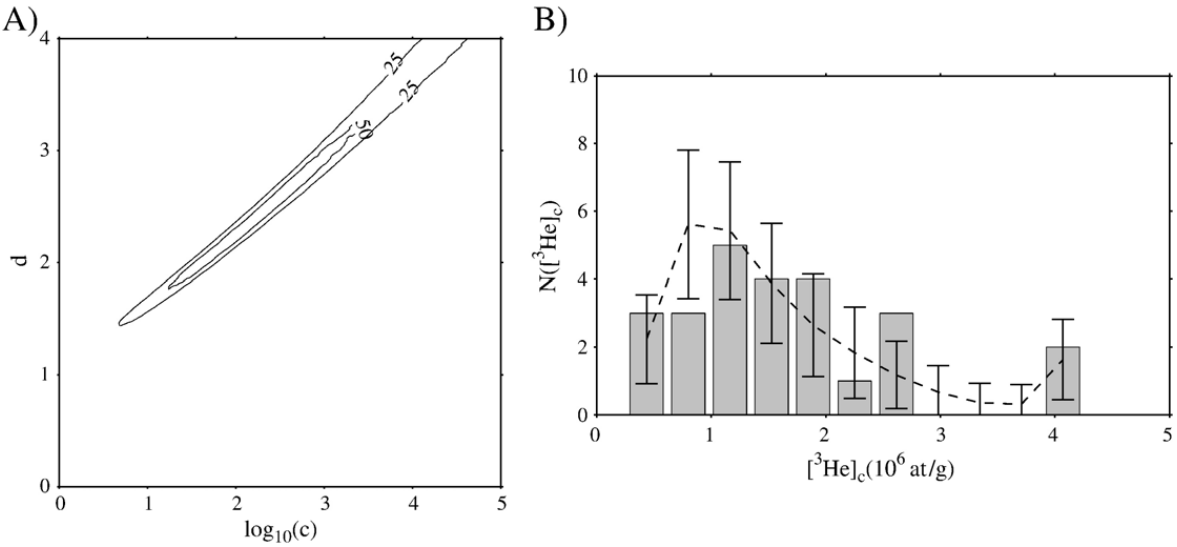

Fig. 5. Frequency distribution modeled using a curvature-dependent erosion function. A) The range of c and d values explored corresponds to the entire scale of the x- and y-axis. For each pair of c and d values, the model was run a 1000 times. For each run, a model distribution of $[^3He]_c$ (see text for explanation) was generated and it was classified as a good fit if it accounted for at least a third of the power in the measured frequency distribution (see text for explanation). The contours represent the percentage of model runs that were a good fit to the observed frequency distribution for a particular value of c and d. Unlike for the slope-dependent case, the 75% contour is not continuous, but rather occurs as discontinuous areas within the 50% contour. Hence, it is not shown. B) Comparison between the observed frequency distribution (histogram in gray) and the modeled frequency distribution (black dashed line) using our best estimate of $c=70$ and $d=2.14$ for Eq. (5). The estimate is based on the largest number of good fits (85%) over the 1000 simulations. The dotted line represents the mean values of each bin from the 1000 Monte Carlo simulations, and the bars represent the corresponding 67% confidence interval.

given c. Reasonable fits to the observed frequency distribution are obtained for values of d between 1.8 and 3.2 but are between 10 and 1000 for the leading coefficient, c. The best estimate of c and d are $c=70$ and $d=2.14$ based on the highest probability instance of 85% over the 1000 Monte Carlo simulations. Model distributions generated using these values of c and d are a good match to the measured $[^3He]_c$ distribution (Fig. 5B), and predict erosion rates in the basin range from ~0 to 4.2 mm/yr, with a mean erosion rate of 0.055 mm/yr. Compared to the slope-dependent erosion function, a larger range of curvature parameters produce distributions that are a fit to the observed distribution. Hence, if erosion rates are controlled by topographic curvature, constraints on the exact form of the parameterized erosion law are weaker. We note that the trends in the parameter space for the slope- and curvature-dependent erosion functions are opposite, although the distributions of slope and curvature across the basin are not anti-correlated. The anti-correlation results from the power law used (Eqs. (4) and (5)) and the relative magnitudes of the slope and curvature values in the Waimea basin, 0 to 4.65 versus 0 to 0.09 m^{-1}, respectively.

We note that our present modeling of the landscape does not incorporate the effects of olivine dissolution. Lava flows exposed in the Waimea basin show no sign of preferential dissolution of olivines, compared to the matrix. Studies of erosion rates in tropical landscapes with basaltic lithology, such as the Deccan traps suggest that rates of chemical weathering (Dessert et al., 2001; Anderson et al., 2005) are less than, or equal to, rates of physical weathering (Anderson et al., 2005). For example, at Réunion, a hotspot volcano in the tropical Indian Ocean and a close analog to the Hawaiian Islands, rates of chemical erosion are a factor of 10–50 lower than rates of mechanical erosion (Louvat and Allègre, 1997). Furthermore, Anderson et al. (2002) suggest that physical weathering sets the pace for chemical weathering, and physical weathering would dominate over chemical weathering in basins that are bedrock dominated, such as the Waimea basin. Hence, olivine dissolution does not affect the overall results of our work and certainly does not impact the new measurement and modeling techniques presented above.

5. Implications

The cosmogenic ^3He measurements indicate an average erosion rate of 0.056 mm/yr. Our estimate of average erosion rate of 0.056 mm/yr for the Waimea basin is comparable to erosion rates from other tropical catchment areas, such as 0.01–0.05 mm/yr in the Deccan traps, and 0.023–0.045 mm/yr in the highlands of Sri Lanka (Hewawasam et al., 2003; von Blanckenburg et al., 2004; Anderson et al., 2005). However, compared to the average precipitation rate of ~100 cm/yr over the entire Waimea basin, average precipitation rates in the Deccan and in the Sri Lankan highlands are higher by a factor of ~2.5 and 4 respectively (von Blanckenburg et al., 2004). Thus, while precipitation may be necessary to drive erosion, the magnitude of precipitation exerts only a weak control on erosion rates in catchment areas not affected by tectonic activity, a conclusion consistent with previous studies. Rather, it is possible that rock strength and fracture density exert a larger control on erosion rates (Anderson et al., 2005).

Modeling of erosion rates in the Waimea basin, however, indicates that a uniform erosion rate across the basin does not explain the measured $[^3He]_c$ in olivine grains. The measured $[^3He]_c$ distribution can be explained if sediment production rates have a non-linear dependence on local topographic curvature or slope. The importance of topographic gradients in controlling erosion rates has been a subject of active study since Gilbert (1877) postulated that the steepest slopes erode more rapidly. The frequency distribution of $[^3He]_c$ provides direct observational evidence for this postulate and our modeling allows us to quantify the relationship between topographic gradients and erosion rates. While our current data set does not allow us to distinguish between slope- and curvature-dependent erosion rates, we suggest a test that in future may allow for such distinction. Fig. 6 shows that although erosion rates in the Waimea basin are highly variable for both cases, the spatial pattern of erosion rates is slightly different. This difference in erosion pattern between the two models provides an opportunity to discern between the slope and curvature based models of erosion (Fig. 6C). Because $[^3He]_c$ is inversely proportional to erosion rate, future $[^3He]_c$ measurements in bedrock samples from the Canyon walls of the Waimea basin could provide the data to test these hypotheses.

The ridges between the river channels in the Waimea basin are formed by incision into the original basaltic surface with the ridgelines likely representing paleosurfaces (also see Seidl et al., 1994). This paleosurface can be traced across the valleys in the basin and all the way to the west coast of Kauai. Therefore, the total incision in the Waimea basin is limited to ~1400 m. Both slope- and curvature-dependent laws yield large spatial variations in erosion rates in the Waimea basin (Fig. 6) with the steepest regions in the basin eroding at the rate of a few mm/yr, more than an order of magnitude higher than the average erosion rate. Erosion rates of a few mm/yr

are common in tectonically active regions (e.g., Vance et al., 2003) but our analyses suggest that such high rates may also occur in drainage basins from tectonically stable regions, albeit locally. However, erosion rates of 1 mm/yr or higher, which we predict to be present on hillslopes in excess of 70°, cannot be sustained in the Waimea basin over a timescale of 4 Myrs since such rates imply incisions of ≥4 km. Hence, our modeling predicts that regions with high topographic gradients in the Waimea basin are transient features.

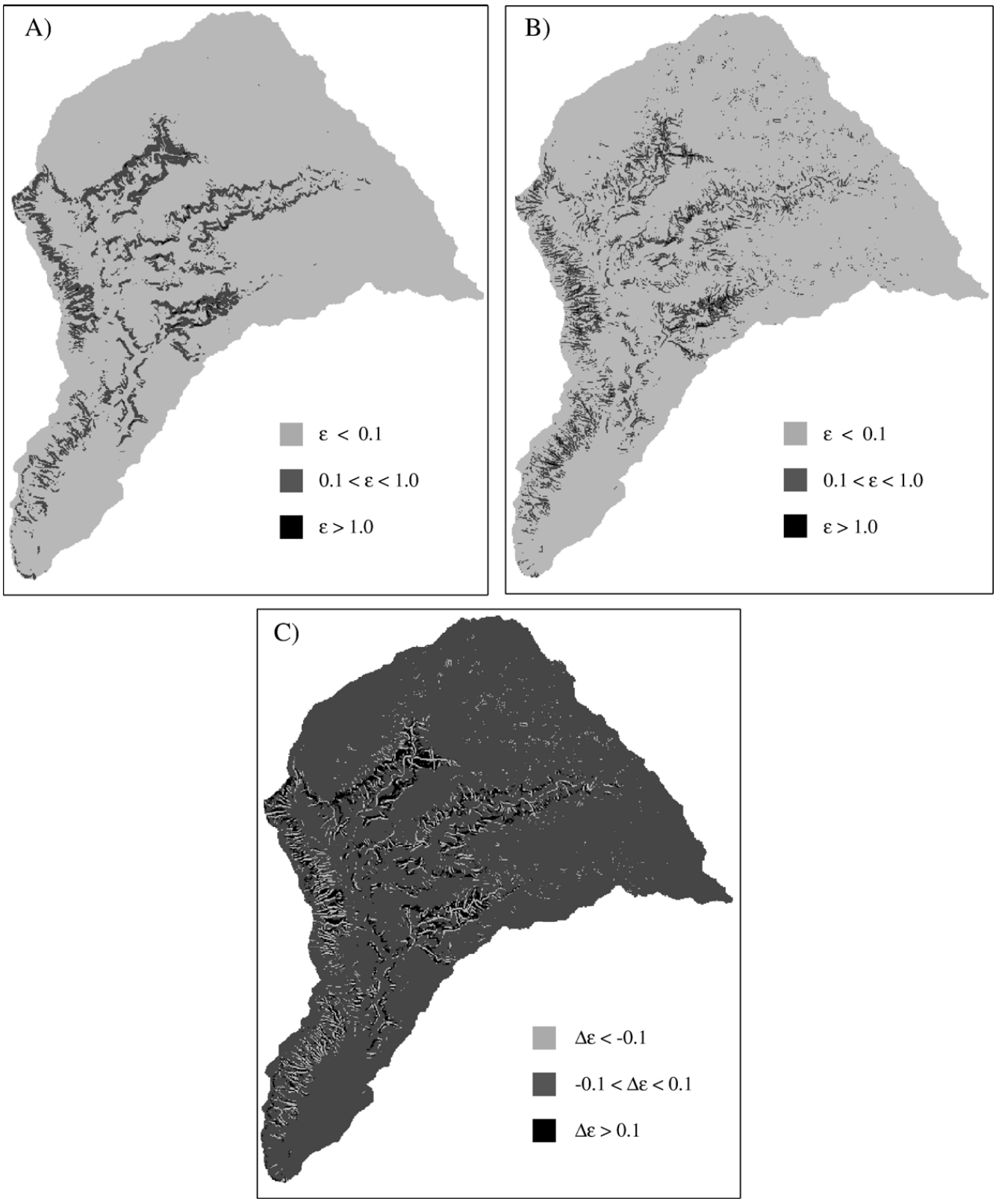

We have presented both new techniques for measuring cosmogenic nuclides in river sediments as well as modeling the observed distributions. Our analyses have shown that sediment production does depend on local topographic gradients and the frequency distribution of cosmogenic nuclides in river sediments can be used to constrain the parameterized forms of erosion laws. Parameterized erosion laws map the physical processes of erosion into approximate numerical expressions that are invaluable for modeling of landscape evolution. Such parameterized equations for sediment generation in regions such as the Himalayas, and the Andes, would be especially valuable at investigating the feedback between tectonics, climate, and landscape evolution. While numerous mechanisms can account for the incision and evolution of fluvial landscapes, two of the most widely considered are the stream power/shear stress (e.g., Howard, 1994; Whipple and Tucker, 1999), and bedload tools/cover models (Sklar and Dietrich, 2006). Stream power/shear stress dependent erosion models posit that the rate of channel incision is limited by the ability of the channel to incise into its bed at a rate that increases, perhaps non-linearly, with local stream power/shear stress. While these empirically constrained erosion laws have not been derived from first order mechanical principles they have proved to provide accurate descriptions of fluvial topography. The bedload tools/cover class of models is based on the first principles calculation of how sediment abrades (tools effect) and protects (cover effect) the underlying channel bed as it saltates downstream. The tools effect increases with bedload flux until the sediment cover is thick enough to protect, or cover, the channel bed from further incision. Both classes of models can be interpreted in terms of the power–law slope dependence of the slope exponent, b. If the slope exponent is interpreted in terms of a bedload erosion model (Sklar and Dietrich, 2006), it implies that the tools effect is dominant and that sedimentary cover effects are not significant enough to limit erosion of the steepest areas of the Waimea watershed, which we estimate to be the most significant contributors to sediments at our sampling location. For the case of a stream power/shear stress erosion rate law a slope exponent of $b=2.3$ is consistent with a shear stress dependence of, $\tau^{3/2}$, and implies relatively weak dependence on lithology and climatic conditions compared to the linear case (Whipple and Tucker, 1999).

While we have demonstrated the ability to constrain spatial variations in sediment generation rates by measuring ^{3}He in small olivine grains (1–3 mm), the technique can be readily adopted for ^{10}Be measurements on 10–100 quartz grains, ranging in diameter from 5 to 10 mm. The ^{10}Be measurements could also be made on single quartz-rich clasts. While olivine is found in restricted environments on the Earth's surface, quartz-rich lithologies are quite common. However, ^{10}Be measurements cannot be used effectively for detrital quartz grains <2 mm in diameter, since many 1000s of grains would need to be analyzed for a single ^{10}Be measurement. Averaging the cosmogenic nuclide concentrations over such a large number of grains would lead to loss of information on the spatial distribution of erosion rates. Cosmogenic ^{21}Ne (^{21}Ne$_c$) measurements could be made on a small number of quartz grains, ~40–50 grains with diameters of 1.5–2.0 mm. However, nucleogenic neon in some cases dominates over the cosmogenic component, although chemical leaching and in-vacuo crushing can isolate the cosmogenic component of neon, albeit with varying degree of success (Niedermann et al., 1994; Hetzel et al., 2002). It is clear that additional technique development with ^{21}Ne$_c$ would be necessary to effectively isolate nucleogenic neon from cosmogenic neon before ^{21}Ne$_c$ can be reliably used in detrital quartz grains. Measurements of $[^{3}\mathrm{He}]_c$ in detrital garnets, or apatite, offers additional minerals that could be utilized for producing frequency distributions of cosmogenic nuclides from river sediments. Obtaining reliable cosmogenic ^{3}He concentrations from these mineral phases may require their crystallization ages to be relatively young, on the order of few to ten million years, as they may contain nucleogenic ^{3}He. Nevertheless, both garnets and apatites are known to be retentive for $[^{3}\mathrm{He}]_c$ and these mineral phases have been successfully used in surface exposure dating (Gayer et al., 2004; Farley et al., 2006).

Finally, it is important to note that by constructing a model for cosmogenic nuclide accumulation and sediment generation rates, the measured frequency distribution in detrital olivine grains from a single locality can be used to map erosion rates over the entire basin (Fig. 6). Detailed spatial patterns of erosion rates would

Fig. 6. A) Map of the Waimea basin showing the distribution of the modeled erosion rate calculated with the slope-dependent erosion function with $a=0.01$ and $b=2.23$. B) Map of the Waimea basin showing the distribution of the modeled erosion rate calculated with the curvature-dependent erosion function with $c=70$ and $d=2.14$. Erosion rates have been binned for both the slope- and curvature-dependent erosion laws and the erosion rates are plotted in mm/yr. C) The predicted difference in erosion rates, in mm/yr, between slope- and curvature-dependent erosion laws. Negative values of $\Delta\varepsilon$ are regions where the curvature based erosion law predicts higher erosion rates than the slope-dependent erosion law; positive values of $\Delta\varepsilon$ are regions were slope-dependent erosion law predicts higher erosion rates. There are significant differences in the erosion patterns for the two erosion laws and in particular, the largest differences are predicted to be present on the canyon walls.

be useful for land management purposes, such as identifying regions that are eroding at high rates and may be susceptible to mass wasting events.

6. Conclusions

We have shown that the frequency distribution of cosmogenic nuclide concentrations in river sediments provides observational constraints on spatial variability of erosion rates within a drainage basin as well as the parameterized form of the erosion laws. Additionally, stochastic sampling of model parameter space allows for the determination of the probability of obtaining a given detrital sample from a predicted parent distribution. Our modeling indicates that for the Waimea basin, a uniform erosion rate is inconsistent with the measured frequency distribution of ^{3}He. However, both slope and curvature-dependent erosion laws with exponents of $\sim$2 are consistent with the observed distribution. Although we currently cannot distinguish between slope and curvature-dependent erosion rates, the spatial distributions of erosion are predicted to be distinct for the two laws. Hence, future cosmogenic ^{3}He measurements in bedrock samples may be able to distinguish between these two parameterized forms of sediment generation rates.

The average erosion rate of the Waimea basin is $\sim$0.05 mm/yr, similar to erosion rates from comparably sized catchment areas in other tropical areas, such as the highlands of Sri Lanka or the Deccan Traps. The Sri Lankan and Deccan catchments, however, have higher precipitation rates. Thus, the similarity of erosion rates suggests that while precipitation is necessary for fluvial erosion, the magnitude of precipitation exerts a weak control on erosion rates in tectonically inactive regions.

Acknowledgements

This work was supported by funds provided to SM by Harvard University. We thank Chuck Blay for his hospitality and for helping with sample collection, and the Hawaii Department of Land and Natural Resources for allowing us access to the sampling site. Careful and thoughtful reviews by David Shuster and Samuel Niedermann helped to improve this manuscript.

References

Anderson, S.P., Dietrich, W.E., Brimhall, G.H., 2002. Weathering profiles, mass-balance analysis, and rates of solute loss: linkages between weathering and erosion in a small, steep catchment. Geol. Soc. Amer. Bull. 114, 1143–1158.

Anderson, S.P., Narayana, A., Anderson, R.S., Molnar, P., 2005. Dilute rivers and low sediment yields in the Western Ghats (Sahyadri): slow erosion of a steep terrain with high rainfall. Eos Trans. AGU, 86 (52), (Fall Meet. Suppl., Abstract H53D-0496).

Andrews, J.N., 1985. The isotopic composition of radiogenic helium and its use to study groundwater movement in confined aquifers. Chem. Geol. 49, 339–351.

Beattie, P., 1993. The generation of uranium series disequilibria by partial melting of spinel peridotite— constraints from partitioning studies. Earth Planet. Sci. Lett. 117, 379–391.

Brown, E.T., Bourlès, D.L., Colin, F., Raisbeck, G.M., Yiou, F., Desgarceaux, S., 1995a. Evidence for muon-induced production of ^{10}Be in near-surface rocks from the Congo. Geophys. Res. Lett. 22, 703–706.

Brown, E.T., Stallard, R.F., Larsen, M.C., Raisbeck, G.M., Yiou, F., 1995b. Denudation rates determined from the accumulation of in situ produced ^{10}Be in the Luquillo Experimental Forest, Puerto Rico. Earth Planet. Sci. Lett. 129, 193–202.

Clague, D.A., Dalrymple, G.B., 1988. Age and petrology of alkalic postshield and rejuvenated-shield lava from Kauai, Hawaii. Contrib. Mineral. Petrol. 99, 202–218.

Dessert, C., Dupré, B., François, L.M., Schott, J., Gailardet, J., Chakrapani, G., Bajpai, S., 2001. Erosion of Deccan Traps determined by river geochemistry: impact on the global climate and the ^{87}Sr/^{86}Sr ratio of seawater. Earth Planet. Sci. Lett. 188, 459–474.

Dunne, J., Elmore, D., Musikar, P., 1999. Scaling factors for the rates of production of cosmogenic nuclides for geometric shielding and attenuation at depth on sloped surfaces. Geomorphology 27, 3–11.

Farley, K.A., Libarkin, J., Mukhopadhyay, S., Amidon, W., 2006. Cosmogenic and nucleogenic He-3 in apatite, titanite, and zircon. Earth Planet. Sci. Lett. 248, 451–461.

Fernandes, N.F., Dietrich, W.E., 1997. Hillslope evolution by diffusive processes: the timescale for equilibrium adjustments. Water Resour. Res. 33, 1307–1318.

Gayer, E., Pik, R., Lavé, J., France-Lanord, C., Bourlès, D., Marty, B., 2004. Cosmogenic ^{3}He in Himalayan garnets indicating an altitude dependence of the ^{3}He/^{10}Be production ratio. Earth Planet. Sci. Lett. 229, 91–104.

Gilbert, G.K., 1877. Report on the geology of the Henry Mountains. U. S. Geog. and Geol. Survey (160p.).

Granger, D.E., Kirchner, J.W., Finkel, R., 1996. Spatially averaged long-term erosion rates measured from in situ produced cosmogenic nuclides in alluvial sediment. J. Geol. 104, 249–257.

Hetzel, R., Niedermann, S., Ivy-Ochs, S., Kubik, P.W., Tao, M., Gao, B., 2002. Ne-21 versus Be-10 and Al-26 exposure ages of fluvial terraces: the influence of crustal Ne in quartz. Earth Planet. Sci. Lett. 201, 575–591.

Hewawasam, T., von Blanckenburg, F.V., Schaller, M., Kubik, P., 2003. Increase of human over natural erosion rates in tropical highlands constrained by cosmogenic nuclides. Geology 31, 597–600.

Howard, A.D., 1994. A detachment-limited model of drainage basin evolution. Water Resour. Res. 30, 2261–2285.

Kennedy, A.K., Lofgren, G.E., Wasserburg, G.J., 1993. An experimental study of trace-element partitioning between olivine, orthopyroxene and melt in chondrules— equilibrium values and kinetic effects. Earth Planet. Sci. Lett. 115, 177–195.

Kent, A.J.R., Rossman, G.R., 2002. Hydrogen, lithium, and boron in mantle-derived olivine: the role of coupled substitutions. Am. Mineral. 87, 1432–1436.

Kurz, M.D., 1986. Cosmogenic helium in a terrestrial igneous rock. Nature 320, 435–439.

Kurz, M.D., Colodner, D., Trull, T.W., Moore, R.B., O'Brien, K., 1990. Cosmic ray exposure dating from in situ produced cosmogenic ^{3}He:

results from young Hawaiian lava flows. Earth Planet. Sci. Lett. 97, 177–189.

Kurz, M.D., Kenna, T.C., Lassiter, J.C., DePaolo, D.J., 1996. Helium isotopic evolution of mauna Kea Volcano: first results from the 1-km drill core. J. Geophys. Res. 101, 11781–11791.

Lal, D., 1991. Cosmic ray labeling of erosion surfaces: in situ nuclide production rates and erosion models. Earth Planet. Sci. Lett. 104, 424–439.

Lal, D., Arnold, J.R., 1985. Tracing quartz through the environment. Proc. Indian Acad. Sci., A Earth Planet. Sci. 94, 1–5.

Louvat, P., Allègre, C.J., 1997. Present denudation rates on the island of Réunion determined by river geochemisty: basalt weathering and mass budget between chemical and mechanical erosion. Geochim. Cosmochim. Acta 61, 3645–3669.

Matmon, A., Bierman, P.R., Larsen, J., Southworth, S., Pavich, M., Finkel, R., Caffee, M., 2003a. Erosion of an ancient mountain range, the Great Smoky Mountains, North Carolina and Tennessee. Am. J. Sci. 303, 817–855.

Matmon, A., Bierman, P.R., Larsen, J., Southworth, S., Pavich, M., Finkel, R., Caffee, M., 2003b. Erosion of an ancient mountain range, the Great Smoky Mountains, north Carolina and Tennessee (vol 303, pg 972, 2003). Am. J. Sci. 303, 972–973.

McDougall, I., 1979. Age of shield-building volcanism of Kauai and linear migration of volcanism in the Hawaiian Island chain. Earth Planet. Sci. Lett. 46, 31–42.

Molnar, P., England, P., 1990. Late Cenozoic uplift of mountain ranges and global climate change: chicken or egg? Nature 346, 29–34.

Mukhopadhyay, S., Lassiter, J.C., Farley, K.A., Bogue, S.W., 2003. Geochemistry of Kauai shield-stage lavas: implications for the chemical evolution of the Hawaiian plume. Geochem. Geophys. Geosys. 4, 1009. doi:10.1029/2002GC000342.

Niedermann, S., Graf, T., Kim, J.S., Kohl, C.P., Marti, K., Nishiizumi, K., 1994. Cosmic-ray produced Ne-21 in terrestrial quartz— the neon inventory of Sierra-Nevada quartz separates. Earth Planet. Sci. Lett. 125, 341–355.

Niemi, N.A., Oskin, M., Burbank, D.W., Heimsath, A.M., Gabet, E.J., 2005. Effects of bedrock landslides on cosmogenically determined erosion rates. Earth Planet. Sci. Lett. 237, 480–498.

Riebe, C.S., Kirchner, J.W., Granger, D.E., Finkel, R.C., 2000. Erosional equilibrium and desequilibrium in the Sierra Nevada, inferred from cosmogenic ^{26}Al and ^{10}Be in alluvial sediment. Geology 28, 803–806.

Ryan, J.G., Langmuir, C.H., 1987. The systematics of lithium abundances in young volcanic-rocks. Geochim. Cosmochim. Acta 51, 1727–1741.

Sarda, P., Staudacher, T., Allègre, C.J., Lecomte, A., 1993. Cosmogenic neon and helium at Réunion: measurement of erosion rate. Earth Planet. Sci. Lett. 119, 405–417.

Scarsi, P., 2000. Fractional extraction of helium by crushing of olivine and clinopyroxene phenocrysts: effects on the ^{3}He/^{4}He measured ratio. Geochim. Cosmochim. Acta 64, 3751–3762.

Seidl, M.A., Dietrich, D.E., Kirchner, J.W., 1994. Longitudinal profile development into Bedrock: an analysis of Hawaiian Channels. J. Geol. 102, 457–474.

Schaller, M., von Blanckenburg, F.V., Hovius, N., Kubik, P.W., 2001. Large-scale erosion rates from in-situ produced cosmogenic nuclides in European river sediments. Earth Planet. Sci. Lett. 188, 441–458.

Sklar, L.S., Dietrich, W.E., 2006. The role of sediment in controlling steady-state bedrock channel slope: implications of the saltation–abrasion incision model. Geomorphology 82, 58–83.

Vance, D., Bickle, M., Ivy-Ochs, S., Kubik, P.W., 2003. Erosion and exhumation in the Himalaya from cosmogenic isotope inventories of river sediments. Earth Planet. Sci. Lett. 206, 273–288.

von Blanckenburg, F., Hewawasam, T., Kubik, P.W., 2004. Cosmogenic nuclide evidence for low weathering and denudation in the wet, tropical highlands of Sri Lanka. J. Geophys. Res. 109, F03008. doi:10.1029/2003JF000049.

Whipple, K.X., 2004. Bedrock rivers and the geomorphology of active orogens. Annu. Rev. Earth Planet. Sci. 32, 151–185.

Whipple, K.X., Tucker, G.E., 1999. Dynamics of the stream-power river incision model: implications for height limits of mountain ranges, landscape response timescale, and research needs. J. Geophys. Res. 104, 17,661–17,674.

Whipple, K.X., Meade, B.J., 2004. Controls on the strength of coupling among climate, erosion, and deformation in two-sided, frictional orogenic wedges at steady state. J. Geophys. Res. 109, F01011. doi:10.1029/2003JF000019.